# Molecular dynamics simulations of shock-compressed single-crystal silicon

Gabriele Mogni,[1] Andrew Higginbotham,[1,*] Katalin Gaál-Nagy,[2,3] Nigel Park,[4] and Justin S. Wark[1]
[1]*Department of Physics, Clarendon Laboratory, University of Oxford, Parks Road, Oxford, OX1 3PU, United Kingdom*
[2]*Via Monte Velino 17, 20137, Milano, Italy*
[3]*Institut für Theoretische Physik, Universität Regensburg, D-93040 Regensburg, Germany*
[4]*AWE, Aldermaston, Reading, Berkshire, RG7 4PR, United Kingdom*
(Received 17 April 2013; revised manuscript received 29 November 2013; published 10 February 2014)

We present molecular dynamics simulations using a Tersoff-like potential of single crystals of silicon shock compressed along the ⟨001⟩ direction. We find an elastic response up to a critical stress, above which the shear stress is relieved by an inelastic response associated with a partial transformation to a new high-pressure phase, where both the new phase (*Imma*) and the original cubic diamond phase are under close to hydrostatic conditions. We study how the fraction of the two phases is related to both their geometry and their enthalpy, and discuss the relevance of the results to previous experimental measurements of the response of silicon to shock compression. We note that the simulations are consistent with shear stress relief provided directly by the shock-induced phase transition itself, without an intermediate state of plastic deformation of the cubic diamond phase, but that the onset of inelastic behavior within the simulations still occurs at considerably higher stresses than found in experiments.

DOI: 10.1103/PhysRevB.89.064104 PACS number(s): 64.60.Ej, 64.70.K−, 62.50.Ef

## I. INTRODUCTION

The response of single crystals of silicon to shock compression has been the subject of study for many years since the seminal work of Gust and Royce [1,2]. The behavior of crystals such as silicon, germanium, and diamond to dynamic loading is of interest for a number of reasons, not least of which is that they can be grown with very high purity. Consequently, it might be thought that the mechanisms (and their thresholds) that underlie their ability to relieve the high shear stresses generated by rapid uniaxial compression would be readily amenable to understanding. However, despite decades of research, this is not the case, and to date detailed knowledge of what occurs at the lattice level when pure cubic diamond (*cd*) materials yield under shock compression remains elusive. The lack of progress in determining the underlying physical processes under shock conditions is in stark contrast to our knowledge of the phase diagram of silicon compressed slowly under hydrostatic conditions: Overall, silicon is now known to exhibit a plethora of 11 distinct stable and metastable crystalline phases at high pressures [3,4]. A tabulation of their crystal properties and pressure ranges over which they exist can be found in Refs. [5,6], and in the references cited therein.

In the shock-wave experiments of Gust and Royce [1,2], the authors observed multiple waves traversing the sample. The first wave corresponds to purely elastic response—the so-called Hugoniot elastic limit (HEL). The second wave was assumed to mark the onset of plastic deformation, allowing the material to relax from an initial state of uniaxial compression (due to the elastic wave), back towards the hydrostat. For the case of the ⟨100⟩ shock orientation, the HEL was measured to be at a stress of $92 \pm 10$ kbar. A third, higher pressure wave at $140 \pm 4$ kbar was identified as probably being due to a polymorphic phase transition to a higher pressure phase. With wave profile measurements alone, a definitive structural identification cannot be made, although the possibility of a $\beta$-Sn structure (which occurs under static hydrostatic loading at around 120 kbar [5,6]) was still deemed implausible on the grounds of density estimations performed on the recovered sample [1,2]. These findings were then independently extended by later extensive investigations [7–9].

Furthermore, a series of time-resolved measurements on the electrical response of the material during the shock-loading process [10–12] revealed a steep monotonic increase in the electrical conductivity, with an onset of metallic-type behavior at pressures close to the HEL, which might conceivably be consistent with a phase transition, given that the first new phase seen under hydrostatic compression (the $\beta$-Sn phase) is metallic. Single-crystal silicon has also been the object of a comprehensive set of laser-based experiments [13–23], which made use of *in situ* time-resolved x-ray diffraction (TXRD) [24] from samples undergoing laser-induced shock compression. Within the subset of these TXRD experiments in which laser-induced pressures exceeding the nominal value of the HEL were achieved, the silicon target appeared to exhibit a purely elastic response, with no observable shifts in the diffraction signals corresponding to the interplanar lattice spacings transverse to the shock propagation direction which would have marked the onset of some form of inelastic or plastic deformation [16,18,20,25]. This "anomalous" elastic response was rationalized [16,18] in terms of the characteristic time scales for the propagation of dislocations in Si, which were estimated to be of order of microseconds, in marked contrast with the nanosecond and picosecond duration of laser-induced shock waves and the rapid deformation response of copper crystals which contain highly mobile dislocations. In addition, the residual structure of recovered samples of laser-shocked single-crystal silicon was itself investigated [26,27]. Similarly to the aforementioned TXRD experiments, these studies proved unsuccessful in detecting evidence for the formation of stable high-pressure phases, suggesting that any phase transition that could have possibly taken place during the loading process was only temporary and was consequently followed upon pressure release by a rapid transformation

*a.higginbotham1@physics.ox.ac.uk

 

back to the original *cd* structure in a highly compressed, polycrystalline state.

On the theoretical front, the shock compression of crystals with the diamond cubic structure has been investigated in a number of classical molecular dynamics (MD) studies. Oleynik and co-workers [28] reported four different regimes of material response as the shock strength increased: simple elastic compression below the HEL, a second plastic wave, an anomalous elastic response above the HEL justified in terms of a nonmonotonic dependence of shear stress on uniaxial compression of the material, and a single overdriven plastic wave inducing amorphization or chemical reactions. On the other hand, Lane and Thompson [29] performed a similar set of simulations of germanium, in which this time they identified the onset of the phase transition to a new body-centered tetragonal structure without an intermediate state of plastic deformation. Similar results were reported by Lin, Perriot, and co-workers [30,31] for the case of diamond.

In the work discussed here we extend certain of the results outlined above. We present MD simulations of single-crystal silicon shock compressed along the ⟨001⟩ direction. In agreement with other work on germanium and diamond [29–31] we find elastic response up until a critical stress, above which the shear stress is relieved by a fraction of the material undergoing a phase transformation. As in the germanium case described by Lane and Thompson [29], in our simulations of shock-compressed silicon we also identify a body-centered lattice in the new phase. However, a reciprocal space analysis of the sample provides more detailed information, and allows us to identify the new phase predicted by this potential to be *Imma*, rather than $\beta$-Sn. We demonstrate that the shock conditions under which the transformation occurs within the simulations can be readily understood in terms of the relative enthalpy of the sample when compressed uniaxially, to that within the mixed-phase region, assuming the material in the mixed phase is close to being in a hydrostatic condition. Furthermore, as the transition is inelastic rather than plastic (in the sense that the shear stress is not relieved by defect generation and motion), not only can the fractions of the phases in the mixed-phase region be readily predicted, but the morphology of the banding structure between the two phases can be understood by considering the lattice parameters of the two phases in the mixed-phase region and the condition of zero transverse strain. However, while our analysis provides a more detailed picture of what occurs at the atomic level within the simulations of shock-compressed silicon, it is the case, as with previous simulations, that the predicted onset of inelastic behavior occurs at stresses considerably higher than those seen in experiment. This may indicate that the potentials being used are still not yet capable of capturing the full pertinent physics, even if the mechanisms being revealed may be hinting at the underlying physics that occurs within such materials under shock compression.

## II. MOLECULAR DYNAMICS SIMULATIONS

The computational technique of classical MD has proven to be an invaluable tool for modeling the response of solids under shock compression [32–34], affording insight at an atomistic level on physical processes that occur under such conditions, such as shock-induced phase transitions [35,36], the nucleation and propagation of dislocations and stacking faults in face-centered cubic materials [37–40], and shock-induced melting [41].

In the work we present here we use the readily available LAMMPS code [42] to perform two sets of MD simulations of uniaxial shock-wave propagation along the ⟨001⟩ direction in single-crystal silicon. Propagation along the two other main symmetry directions in the sample, ⟨011⟩ and ⟨111⟩, has not been considered in the context of the research presented in this paper, and is indeed worthy of future investigation. The first set of smaller simulations, which we shall henceforth refer to as set I, was used for those tasks in which the final results sought were deemed to be relatively size independent, and therefore the speed of the simulation was of high priority, whereas the second set (set II) were much larger simulations, employed when the overall stability of the wave profiles was the most important criterion. In both sets, shock waves with propagation velocity $U_S$ were launched into the system by the impact of a piston only a few unit cells wide and with constant atomic velocity $U_p$, following the initial thermalization of the bulk sample at 300 K for 3 ps. Periodic boundary conditions were imposed on the two dimensions transverse to the shock-propagation direction. The interatomic interactions in the sample were modeled with a modified semiempirical bond-order Tersoff-like potential [43–45], as parametrized by Erhart and Albe [46], which has in the past been compared with alternative potentials [47–49] and has proven successful in describing various properties of crystalline silicon including elastic constants [50] and general thermodynamic properties [51], as well as the properties of the *cd* to $\beta$-Sn phase transition under both hydrostatic and uniaxial compression [52–54]. In set I, the sample cross section was $30 \times 30$ unit cells, and 390 unit cells along the shock-wave propagation direction (the $z$ axis), corresponding to a total of 2 809 800 atoms. For all values of $U_p$, the elastic shock front reached the rear end of the sample and underwent reflection just after 23 ps from the start of the simulations, and unless otherwise stated 23 ps is the time when results from the set I simulations are presented in everything that follows. In set II, the sample dimension was of $100 \times 100 \times 1500$ unit cells, corresponding to 120 020 000 atoms in total. Piston velocities between $U_p = 1.4$ km s$^{-1}$ and $U_p = 2.5$ km s$^{-1}$ in steps of 0.1 km s$^{-1}$ were explored in both cases. Finally, it is worth emphasizing that all samples considered in this work have been modeled as perfect defect-free crystals, given that silicon can be manufactured with essentially zero defect density [55].

A typical simulation from set I for a particle velocity of 1.6 km s$^{-1}$ is shown in Fig. 1, where the atoms have been color coded according to their centro-symmetry parameter (CSP) [56]. An elastic precursor is observed, followed by a region of bands of interlocking parallelepipeds composed (as we demonstrate below) of material in the *Imma* phase, and lying inclined at an angle relative to the sides of the simulation box across the (111) crystallographic plane of the compressed sample. Only two such planes of the banding structure are activated in the set I simulations due to the deliberately restrictive size of the cross-sectional area, whereas in the larger set II simulations all four planes have been observed to be activated. The set I simulations therefore afford for a

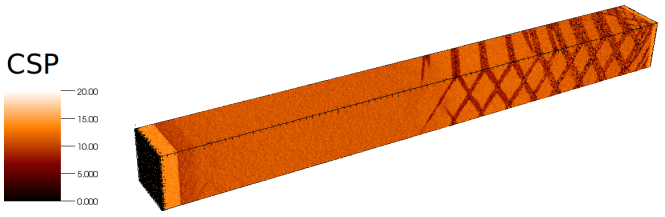


FIG. 1. (Color online) Example of a set I simulation of shock-wave propagation (from right to left) in single-crystal Si at a particle velocity of 1.6 km $s^{-1}$, and 23 ps after the start of the simulation. The atoms are color coded according to their CSP [56]. The CSP is higher for the material in the *cd* phase depicted in light orange (around 11.5 $Å^2$) than for the remaining *Imma* phase shown in darker red (around 6 $Å^2$). Note that at the points where the bands of *Imma* phase intersect the value of CSP drops to nearly zero (colored in black), possibly as a result of stress-concentration effects. The structure of intersecting parallelepipeds of *Imma* material that constitutes the mixed-phase region is clearly visible, together with the region of elastic compression that precedes it.

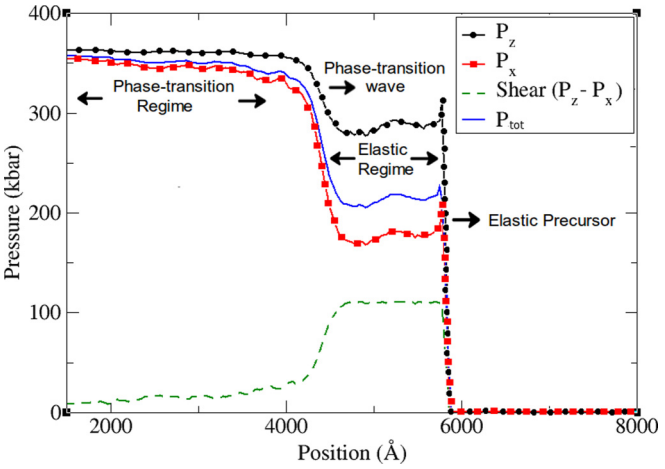


FIG. 2. (Color online) Wave profiles as a function of position in the sample of the pressure components $P_x$ and $P_z$, together with those of the total pressure $P_{\rm tot} = \frac{1}{3}(P_x + P_y + P_z)$ and the shear stress $P_z - P_x$, for the set II simulation at $U_p = 1.9$ km $s^{-1}$. The positions of the elastic precursor front and the ensuing phase transition wave are indicated.

cleaner and simpler picture of the banding structure, and for this reason much of the ensuing analysis of the microstructure of the phase transition presented in the remainder of this paper will be performed on these smaller simulations. The larger set II simulations on the other hand are not readily amenable for structural analysis due to the complicated nature of the banding structure observed there. Qualitatively however, the same phenomena are observed to occur in the two sets of simulations, including the shock-induced phase transition and the ensuing relief of shear stress, and both sets therefore offer the same degree of physical insight into these phenomena. The onset of the mixed-phase banding structure was first detected at a particle velocity of 1.6 km $s^{-1}$ in the set I simulations, and slightly lower at 1.5 km $s^{-1}$ in the set II simulations. It was then observed to dominate the response of the sample up to around 2.1 km $s^{-1}$, at which point it started to be gradually eroded by shock-induced melting (which was confirmed by the onset of considerable diffusion of individual atoms). In most of the results that follow (unless otherwise stated) we will therefore restrict the analysis to values of $U_p$ below 2.3 km $s^{-1}$, before melting becomes significant. The two-wave profile in the stress due to the phase transformation is shown in Fig. 2, together with the evolution of the residual shear stress as a function of distance, for a shock of particle velocity 1.9 km $s^{-1}$. We find that the degree of relief of the shear stress increases as a function of particle velocity $U_p$, as shown in Fig. 3, until it eventually vanishes altogether at the onset of the shock-induced melting. As explained earlier, the set I simulations were used to perform most of the analysis on the microstructure due to the simplicity of the banding structure there. In particular, the region of the simulations encompassing the stable part of the pressure and particle velocity profiles, with a typical width of 300 Å, was considered for performing this analysis. Longer simulations were used to confirm that the final states reached were indeed stable on the time scales accessible to simulation. We have also made a spot check of the normal component of the pressure on either side the interface between the two phases and found that they agree within 3%, further confirming that the mixed-phase system is close to equilibrium

As noted above, we identify the mixed-phase region to be composed of close-to-hydrostatically compressed *cd* and *Imma* phases. The identity of the two phases was confirmed by separating them by internal energy per atom (they can also be readily separated by CSP), calculating the Fourier transform (FT) of the atomic coordinates, and analyzing the resulting diffraction pattern [57]. The lifting of symmetry in the basis of *Imma* leads to a reappearance of peaks in the FT which are forbidden by the cubic diamond (and by extension $\beta$-Sn) structure factor. The presence of these peaks in the FT,

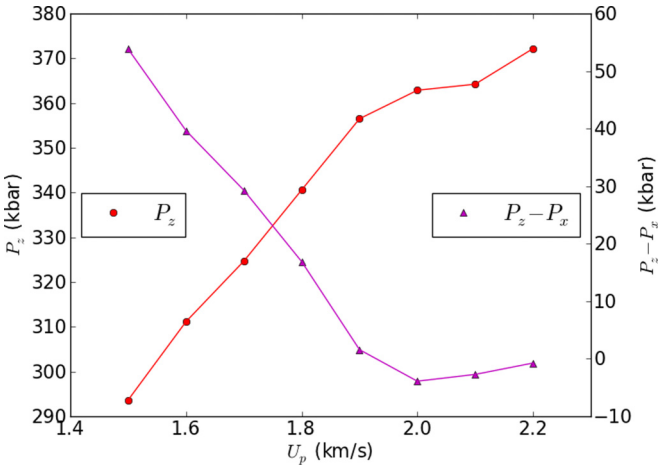


FIG. 3. (Color online) Values from the set II simulations of the pressure component $P_z$ and of the residual shear stress $P_z - P_x$ across the stable part of the phase transition wave. The magnitude of the shear stress at the end of the phase transformation process gradually decreases from the first occurrence of the phase transition at 1.5 km $s^{-1}$, until it is essentially fully relieved by $U_p = 2.0$ km $s^{-1}$ as a result of the onset of the new liquid phase.

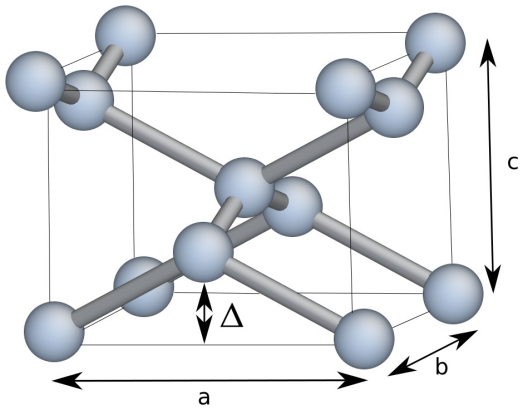


FIG. 4. (Color online) Four-atom unit cell of the orthorhombic *Imma* phase, where $a$, $b$, and $c$ are the lattice parameters and $\Delta$ is the degree of freedom in the atomic position of the second atom in the two-atom basis at $(0, \frac{1}{2}, \Delta)$.

along with analysis of the real space structure, confirm that the transformed material lies in the *Imma* phase, not the closely related $\beta$-Sn.

An analysis of reciprocal space therefore confirms that the mixed-phase region, following the region of elastic compression, is comprised of nearly hydrostatically compressed silicon in a high-pressure *cd* structure and of material in the high-pressure *Imma* phase [58,59]. This new phase has a body-centered orthorhombic (bco) Bravais lattice, with a two-atom basis with atoms at the origin (0,0,0) and at atomic position $(0, \frac{1}{2}, \Delta)$, where $\Delta$ ranges between 0.25 and 0.5. The significance of this $\Delta$ parameter relative to the conventional four-atom unit cell of the *Imma* phase is shown in Fig. 4. A summary of the special values that the four parameters of this cell, $a$, $b$, $c$, and $\Delta$, take in each of the phases is presented in Table I.

The overall appearance of the banding of this mixed-phase region is qualitatively very similar to the results reported by Lane and Thompson [29] in their simulations of shock-compressed germanium. In agreement with their results, we find that rather than defect-mediated plasticity, it is the phase transition itself that relieves the shear stress in the uniaxially compressed lattice—what might be termed an inelastic, rather than plastic response. Indeed, an analysis of the mixed-phase region in reciprocal space shows its usefulness in distinguishing between defect-mediated plasticity, and inelastic behavior. As the material is compressed under conditions of uniaxial strain, the total strain transverse to the shock propagation direction is zero. For any general material response, this means that the total strain transverse to the shock ($\epsilon^T_{\mathrm{Tot}}$) composed in principle of both elastic strain $\epsilon^T_e$ and plastic strain $\epsilon^T_p$ is zero. That is to say $\epsilon^{T=\epsilon^T_e+\epsilon^{T=0}_p}_{\mathrm{Tot}}$. In the case of defect-mediated plasticity in the absence of a phase transition, it is the finite plastic strain $\epsilon^T_p$ caused by the generation and motion of defects that gives rise to a negative elastic strain transverse to the shock propagation (i.e., a compression of the mean spacing of the lattice in this direction). As the lattice is already compressed along the direction parallel to the shock propagation, this results, for an initially cubic material, in the average unit cell changing from being tetragonal (under elastic compression) back to cubic yet further compressed—and thus the material is closer to the hydrostat. As with x-ray diffraction, an FT of the material reveals the elastic strain (owing to the random nature of the defects, which thus do not contribute in large amplitude to the FT signal).

TABLE I. Crystallographic structural parameters of the four-atom unit cell for the three phases considered in this work.

| Structure | $b/a$ | $c/a$ | $\Delta$ | Space Group |
|---|---|---|---|---|
| Cubic Diamond | 1 | $\sqrt{2}$ | 0.25 | $Fd\bar{3}m$ |
| $\beta$-Sn | 1 | free | 0.25 | $I4_1/amd$ |
| *Imma* | free | free | free | *Imma* |

The mechanism behind the inelastic behavior observed here is qualitatively different. In this case, there is no defect mediated plasticity, and thus $\epsilon^T_p$, and hence $\epsilon^T_e$, are both zero. The relief of the shear stress occurs directly due to the phase transition. The new phase (in this case *Imma*) has a lattice spacing in the transverse direction which is larger than the lattice spacing of the unshocked *cd* phase, and thus the transformation of material to the *Imma* phase necessitates a reduction in the lattice spacing of the *cd* phase, driving it towards the hydrostat. We can decompose the total elastic strain in the transverse direction into the elastic strain within the *Imma* and *cd* phases, $\epsilon^T_{e,Imma}$ and $\epsilon^T_{e,cd}$, where now $\epsilon^T_{e,Imma} + \epsilon^T_{e,cd} = 0$.

This interpretation is readily borne out by an analysis of the mixed-phase region in reciprocal space. Figure 5 shows a slice through reciprocal space ($k$ space) across the $k_z = 0$ plane.

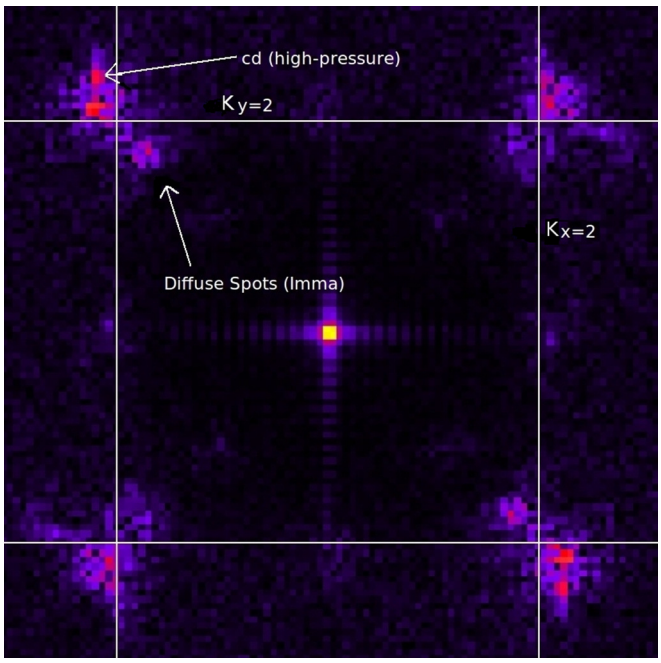


FIG. 5. (Color online) Fourier transform image of the real-space atomic positions in the mixed-phase region. The region shown is the $k_z = 0$ plane between the $k_x \pm 3$ and $k_y \pm 3$ limits (the $k$ axes of the reciprocal plane are in units of $2\pi/a_o$, where $a_o$ is the lattice constant of the uncompressed cubic diamond structure). The equilibrium positions of the {220} diffraction spots are highlighted. The signals corresponding to the two phases on both sides of each of these spots are also labeled.

Note that each of the original (220) reflections has split in two, and are located either side of the position of the (220) reflection of the unshocked material (which we have confirmed is also the position of the peak for the material in the region which is elastically compressed). The generation of this FT using only atoms in the *Imma*, and then *cd*, phase, confirms that the intensity in reciprocal space further from the origin is due to the atoms in the *cd* phase (their lattice spacing has reduced in real space, thus increased in reciprocal space), whereas the intensity closer to the origin is due to the *Imma* phase. Inelastic behavior, as discussed above, is confirmed by the fact that the weighted mean of the intensity remains at the original (220) position, which would not be the case in a situation of defect-mediated plasticity (as observed by Bringa and co-workers for Cu [37]).

## III. MORPHOLOGY OF THE MIXED-PHASE REGION

As noted above, we find that the shear stress in the mixed-phase region is relieved due to the phase transformation: A contraction of the lattice parameter of the *cd* material transverse to the shock is accommodated by the larger lattice parameter in this direction of the *Imma* phase, with the total number of unit cells transverse to the shock propagation direction remaining constant. In this model, a greater fraction of the new phase will allow for a larger accommodation of shear strain, and as such, the fraction of *Imma* will increase with pressure.

We now establish the relation between the condition of relief of shear stress within the mixed-phase region and its microstructure. We will refer to the coordinate system shown in Fig. 6 to describe the orientation of the planar surfaces of a single representative parallelepiped of *Imma* phase in the mixed-phase banding structure. We will also assume for simplicity that all individual unit cells have their sides aligned with the axes of this coordinate system. The angles $\theta$ and $\phi$, which describe the inclination of the parallelepipeds, are therefore related to the lattice parameters $a$, $b$, and $c$ of the orthorhombic unit cell of the *Imma* phase according to the following equations:

$$\tan\theta = \frac{b_I}{c_I}, \quad \tan\phi = \frac{a_I}{c_I}, \qquad \sin\theta = \frac{b_I}{\sqrt{b_I^2 + c_I^2}}, \quad \cos\theta = \frac{c_I}{\sqrt{b_I^2 + c_I^2}}. \tag{1}$$

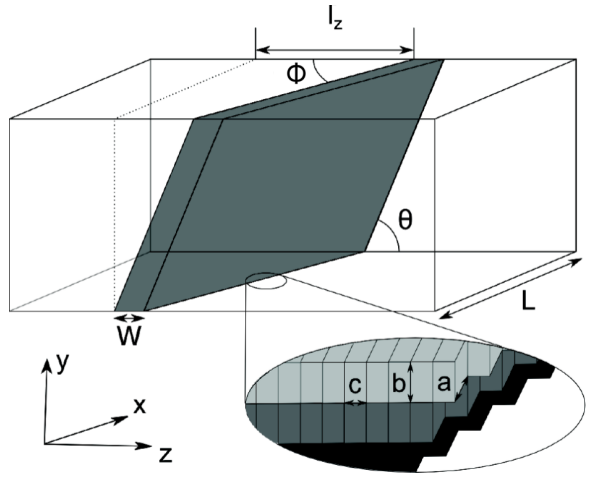


FIG. 6. (Color online) Reference system employed in this study to describe the orientation of a parallelepiped of *Imma* material (shown in dark gray): $x$, $y$, $z$ are the orthogonal Cartesian axes, $\theta$ and $\phi$ are the angles that the parallelepiped makes to the sides of the simulation box containing it, $W$ is the thickness of the parallelepiped, and $L$ is the square cross-sectional dimension of the box. The inset below the figure shows how the individual *Imma* unit cells are stacked on top and next to each other. Only one parallelepiped is shown here for representative purposes, but in the actual simulations the box, of length $l_z$ along the $z$ axis, contains the volume of exactly four such parallelepipeds.

Let us assume full relief of shear stress within the cubic diamond phase, i.e., that $a_{cd} = b_{cd}$ (note that henceforth, *cd* should be understood to refer to the high-pressure cubic diamond material unless otherwise stated). At this stage we are left with three degrees of freedom which the parallelepipeds can adopt to accommodate the relief of shear stress: angles $\theta$ and $\phi$, and the band width $W$, as defined by Fig. 6. As the shock is uniaxial, we impose conservation of the transverse dimension of the sample, and conservation of transverse number of unit cells. Being limited to the $x$-$y$ transverse plane, the model presented here does not provide any information about the $z$ dimension of the sample. The first condition of conservation of transverse length between the initial unshocked lattice in the equilibrium *cd* structure and the final mixed-phase state can be expressed as

$$N_I a_I + N_{cd} a_{cd} = N_0 a_0 \Rightarrow L_I + L_{cd} = L_0. \tag{2}$$

$N_I$, $N_{cd}$, $N_0$ and $a_I$, $a_{cd}$, $a_0$ are, respectively, the number of unit cells and lattice parameter for the *Imma* phase, *cd* phase, and the unshocked material, along either the $x$ or $y$ direction. The second constraint, namely that the number of unit cells along these directions transverse to the shock is conserved, implies

$$N_0 = N_I + N_{cd}. \tag{3}$$

Considering these two constraints simultaneously we find

$$\frac{L_0}{a_0} = \frac{L_I(a_{cd} - a_I) + L_0 a_I}{a_{cd} a_I}, \tag{4}$$

where

$$L_I = \frac{W}{2} \frac{1}{\sqrt{a_I^2 + c_I^2}} \sqrt{2a_I^2 + \frac{a_I^4}{c_I^2}}, \tag{5}$$

where by symmetry we have assumed $a_I = b_I$. However, even with $a_I = b_I$ the *Imma* unit cell remains different from that of $\beta$-Sn due to the $\Delta$ factor described in Fig. 4.

The prediction that $a_I = b_I$ is supported by the MD simulations, in that we find the values of $a_I$ and $b_I$ extracted directly from the position of the (220) diffraction spot in the FT of the *Imma* phase to be in excellent agreement at a value of around 6.7 Å in all simulations. Moreover, the angles $\theta$ and $\phi$ are found to agree very closely. If the *Imma* phase lay precisely on the hydrostat, then $c_I/a_I \approx 0.55$ for all piston velocities, and we would predict that $\theta = \phi \approx 62^\circ$ according to Eq. (1). In practice, we find that owing to the finite residual shear stress

present in the simulations, $\theta$ and $\phi$ range from around 55° to around 60° as the particle velocity is increased from 1.6 to 2.1 km s$^{-1}$.

As well as the angles that the bands make, the assumption of inelastic deformation allows us to predict the volume fractions $f_I^V$ and $f_{cd}^V$ of *Imma* and *cd* phases, respectively, in the mixed-phase region. We first require an expression for $f_I^V$ in terms of the lattice parameters of the *Imma* unit cell. The volume of a single parallelepiped is in general given by $L_0^2 W$. Hence the volume fraction of a parallelepiped of *Imma* material relative to the volume of the box enclosing it (of length $l_z$), as defined in Fig. 6, is

$$f_I^V = \frac{V_I}{V_{\text{Tot}}} = \frac{W}{l_z}. \tag{6}$$

We thus find that the *Imma* volume fraction of a single parallelepiped within the volume of the box of Fig. 6 is given by

$$f_I^V = \frac{(a_0 - a_{cd})a_I}{2(a_I - a_{cd})a_0} \frac{\sqrt{a_I^2 + c_I^2}}{\sqrt{2c_I^2 + a_I^2}}. \tag{7}$$

Each box of this size contains the volume of exactly four parallelepipeds. An expression for $f_I^V$ accounting for this is given by

$$\left(f_I^V\right)_{\text{Tot}} = \frac{2(a_0 - a_{cd})a_I}{(a_I - a_{cd})a_0} \frac{\sqrt{a_I^2 + c_I^2}}{\sqrt{2c_I^2 + a_I^2}}. \tag{8}$$

A value for the number (rather than volume) fraction of each phase is easily extracted from the MD simulation by binning according to internal energy. Once plotted, the distribution of internal energy appears as a well defined double-peaked distribution, with each peak corresponding to one of the two phases. Also present at the highest values of the internal energy in the overall profile is a smooth distribution of atoms identified as lying at the boundaries between the two phases. These atoms have the highest energy because they are in the most highly strained environments. In counting the number fraction of the *Imma* phase, the number of atoms under the corresponding peak was divided by the total number of atoms across the entire internal energy profile, including therefore the number of atoms at the boundaries, due to these atoms being non-negligible in number. The upper limit in the value of the number fraction for each piston velocity was estimated by assuming that all atoms at the boundaries belong to the *Imma* phase, whereas the lower limit was obtained conversely by assuming that all boundary atoms lie in the *cd* phase. Furthermore, the expression for the volume fraction of Eq. (8) can be converted to a number fraction of atoms in the *Imma* phase $f_I^N$ by noting that

$$f_I^N = \frac{f_I^V V_{cd}}{V_I - f_I^V V_I + f_I^V V_{cd}}. \tag{9}$$

In Fig. 7 we compare the number fractions derived from MD with those calculated from Eq. (9). The lattice parameters used in Eq. (9) were derived from an analysis of the reciprocal space plots for the two phases. By considering a sample of around 20 diffraction spots in reciprocal space for each phase, a statistical analysis on the values of these lattice parameters was performed, with the error bars shown representing the derived standard deviation in number fraction. It can be seen that the values obtained from the model and the MD simulations are consistent for all values of $U_p$.

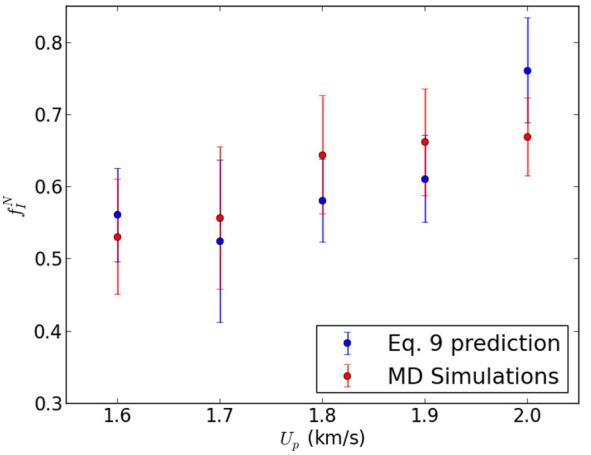


FIG. 7. (Color online) Comparison between the number fraction of the *Imma* phase $f_I^N$ predicted by Eq. (9), with those derived from the set I simulations. MD number fractions were calculated by separating the two phases according to their internal energy.

Despite the consistency between the model and the simulations, it should be noted that the arguments put forward above do not take into account a number of factors. First, we have neglected the effects of lattice rotations, which have been observed in the FT of both phases. These rotations amount to roughly 10° about the $y$ axis for the *cd* phase, and up to around 18° in the opposite sense for the *Imma* phase. We also neglect the effects of interfacial strains occurring at the boundary between *cd* and *Imma* phases. The mismatch in lattice parameters of these two phases will necessarily lead to an incommensurate boundary which could lead to distortion of the simple structures discussed above. However, the highly disordered nature of this boundary material (typically accounting for around 10%-15% of the atoms) makes characterization of these regions highly challenging. In addition, similar issues are encountered at intersections between bands, where once again detailed analysis is hindered by the small number of atoms (rendering reciprocal space analysis ineffective), as well as inherent disorder and strain gradients. We therefore conclude that although quantitative agreement is not to be expected, the qualitative trend exhibited is indicative of the underlying mechanisms conforming to those forming the basis of Eq. (9).

## IV. THERMODYNAMICS OF THE MIXED-PHASE REGION

Under the conditions of constant temperature and pressure such as those predicted to be found in shock-induced mixed-phase regions [60,61], the condition of relative stability between phases is given by the minimization of the Gibbs free energy $G$ of the material

$$G = E + PV - TS, \tag{10}$$

where $E$ is the internal energy, $P$ is the pressure, $V$ is the volume, $T$ is the temperature, and finally $S$ is the entropy. The same considerations apply when comparing the mixed-phase region with the state of elastic compression, except that the definition of $G$ under uniaxial compression is given by [61]

$$G^{\text{uniaxial}} = E + P_z V - TS. \tag{11}$$

In what follows, we shall neglect the entropic contributions to the Gibbs free energies embodied by the term $TS$, so that $G$ reduces to another thermodynamic potential function, that is the enthalpy:

$$H = E + PV, \tag{12}$$

or equivalently

$$H = E + P_z V, \tag{13}$$

for the case of uniaxial compression. We find this assumption to be reasonable given the high stiffness of both the *cd* and *Imma* phases. Within the approximation that the thermal contribution to the entropy can be reasonably evaluated by assigning an Einstein frequency to each phase, and then using the Einstein model, the change in the $TS$ term was found to be of order 25 meV for the *cd* phase and around 40 meV for *Imma*, and therefore small compared with $\Delta H$ in both cases. The configurational entropy due to the banding is clearly negligible. The $TS$ term in the Gibbs free energy is consequently also negligible despite the considerable magnitude of the shock-induced rise in temperature, which is of order $10^3$ K. The effects of temperature are not however completely left out of the enthalpy calculation, since they still significantly contribute to both the internal energy $E$ and pressure $P$ terms.

A complete thermodynamical analysis of the shock-loading process as seen in the MD simulations also requires knowledge of the state variables of the system. These are given by the Rankine-Hugoniot equations embodying the principles of conservation of mass, energy, and momentum across a shock discontinuity:

$$\begin{aligned} \rho_0(U_S - U_0) &= \rho(U_S - U_p), \\ \rho_0(U_S - U_0)(U_p - U_0) &= P - P_0, \\ e - e_0 &= \frac{PU_p - P_0U_0}{\rho_0(U_S - U_0)} - \frac{1}{2}\left(U_p^2 - U_0^2\right), \end{aligned} \tag{14}$$

where $P$ is the external pressure exerted on the material by the shock, $\rho$ is the density, $T$ is the temperature, $U_p$ is the particle velocity, $U_S$ is the shock velocity, $U_0$ is the upstream flow velocity, $e$ is the specific internal energy, and subscript 0 denotes the initial value of each of these variables in the region ahead of the shock front. In addition to the Rankine-Hugoniot equations, the material behavior under shock compression is described by its equation of state (EOS), from which one can derive a $U_S$-$U_p$ relation for the material. For most materials we can employ a linear $U_S$-$U_p$ relation of the form

$$U_S = C_0 + C' U_p. \tag{15}$$

The Rankine-Hugoniot equations lead to the following expression for the jump in specific enthalpy across the shock wave from the equilibrium state, known as the Hugoniot relation [62]:

$$\Delta h = \tfrac{1}{2}(U_p - U_0)(2U_S - U_p - U_0). \tag{16}$$

In the case of a two wave shock we consider each waves' enthalpy contribution in turn. For the leading elastic wave, which is found to travel at velocity $U_S^e = 9.064$ km s$^{-1}$ regardless of pressure, and for which the upstream flow velocity is zero, we can express the enthalpy jump as

$$\Delta h^e = \frac{U_p^e}{2}\left(2U_0 - U_p^e\right), \tag{17}$$

where $U_p^e$ is the particle velocity in the elastically compressed region. Note that this quantity is distinct from, and lower than, the applied piston velocity $U_p$, which will dictate the particle velocity in the phase-changed region behind the second wave. It is found that in the set II simulations these velocities obey the linearity of the $U_S$-$U_p$ relation.

The enthalpy change due to the phase transformation wave can be calculated by noting that the second wave now travels into the elastically compressed region where the flow velocity $U_0 = U_p^e$. This leads to an enthalpy change of

$$\Delta h^p = \tfrac{1}{2}\left(U_p - U_p^e\right)\left(2U_S^p - U_p - U_p^e\right), \tag{18}$$

where we again fit the set II data to find a linear relation between shock and piston velocity for the phase transformation wave. The total enthalpy change for the two wave shock is therefore $\Delta h = \Delta h^e + \Delta h^p$. A summary of the parameters in the $U_S$-$U_p$ relation of the two waves, the elastic and phase transition waves, is offered in Table II.

Finally, a further estimate of the enthalpies for each of the two phases in the mixed-phase region was obtained by directly computing the total average energy and pressure from the MD simulations, and by estimating the atomic volume from the FT patterns. When calculating the enthalpies of the two phases, the pressure in each phase was assumed to be hydrostatic, such that the elementary definition of enthalpy $H = U + PV$ could be used. The individual enthalpies of the *cd* and *Imma* phases were finally weighted by their number fraction predicted from the corresponding lattice parameters according to Eq. (8) for calculating $f_I^V$, together with Eq. (9) for converting from $f_I^V$ to $f_I^N$ (with $f_{cd-hp}^N$ given by $1 - f_I^N$). The total high-pressure mixed-phase enthalpy is consequently given by

$$H_{\text{Tot}}^{\text{HP}} = f_{cd-hp}^N H_{cd-hp} + f_I^N H_I, \tag{19}$$

where $H_i = E_i + P_i V_i$ for a general phase $i$. The final outcome of the two approaches for calculating the total enthalpy jump

TABLE II. Particle and shock velocities $U_p$ and $U_S$ across the elastic and phase transition waves according to the linear $U_S$-$U_p$ relation $U_S = C_0 + C' U_p$. The top value in the column of $C_0$ parameters corresponds to the sound velocity in the material at zero pressure.

| | $C_0$ (km s$^{-1}$) | $C'$ |
|---|---|---|
| $U_p^e$ | 9.064 | 0 |
| $U_S^e$ | 1.1983 | 0.0899 |
| $U_p^p$ | 0 | 1 |
| $U_S^p$ | 2.8401 | 2.048 |

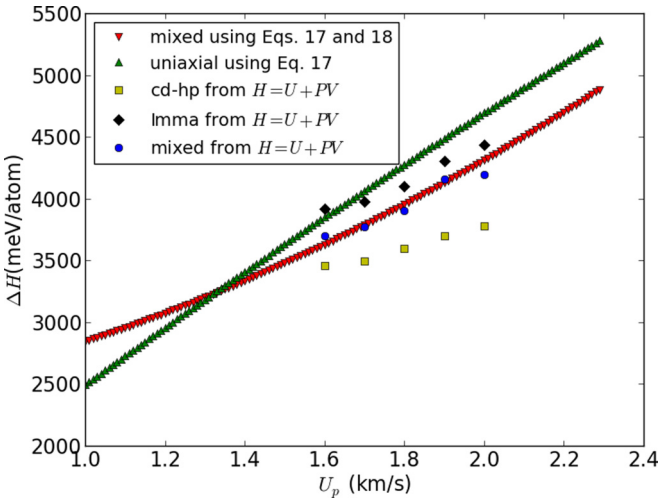


FIG. 8. (Color online) Enthalpy change $\Delta H$ from equilibrium per unit atom as a function of $U_p$ predicted by the various enthalpy extraction methods. The data above $U_p = 2.0$ km s$^{-1}$ is included for completeness but should be treated with caution due to the onset of shock-induced melting in the sample.

across the phase transition from the initial equilibrium state, namely the $U_S$-$U_p$ relation method based on Eq. (16) and the method based on the direct extraction of data from the simulations, is presented in Fig. 8. It can be seen that the overall enthalpy increase predicted by the two different methods are in excellent agreement, confirming that our MD simulations of shock waves obey the Hugoniot relation.

Furthermore, when extrapolating the enthalpy to lower particle velocities, both methods suggest that the shock-induced phase transition to *Imma* should first occur in the range of $U_p$ between 1.3 and 1.4 km s$^{-1}$, where the enthalpy of the mixed-phase region first becomes lower and therefore more thermodynamically favorable than that of the state of elastic uniaxial compression. The first hints of the phase transition were seen at 1.6 km s$^{-1}$ in set I, and at 1.5 km s$^{-1}$ in the larger set II simulations—that is to say in reasonable agreement with the enthalpy analysis. The slightly higher values of $U_p$ found in practice could be linked to the enthalpy barrier between the two regions, which has not been explored here.

Although we find good agreement between the enthalpy determined by the Hugoniot relation and the wave velocities, and that found by directly determining $U$, $P$, and $V$ from the MD simulations, we caution that there remain aspects of the simulations that are still not understood. Most noticeably, we find that the pressures within the two phases are not the same—with the pressure in the *cd* phase being considerably lower than that in the *Imma* phase. Indeed, it is for this reason that the enthalpy of the *cd* phase, shown in Fig. 8, is the lower of the two phases—if the pressures were the same, we would expect the new *Imma* phase to have the lower enthalpy.

We also note that the Hugoniot relation for the shock does provide some modest insight into a potential synergy between the inelastic behavior—in terms of the stress relief being provided by the partial phase transformation—and the minimization of the enthalpy. We see that the Hugoniot relation [Eq. (16)] determines that if the two phases in the mixed-phase region are at the same hydrostatic pressure, then at the first point where the transformation can occur—where we expect the enthalpy per atom of each phase to be identical—we predict that the volume fraction of each phase should be proportional to the enthalpy increase in that phase.

## V. CONCLUSIONS

We have conducted an investigation into the mechanism underpinning the relief of shear stress in shock-compressed single-crystal silicon. Multimillion atom simulations of shock-wave propagation in a single-crystal sample of silicon predict the onset of a high-pressure mixed-phase region following directly after the initial elastic response, consisting of nearly hydrostatically compressed cubic diamond crystal structure and of phase-transformed material lying in the *Imma* high-pressure phase. This mixed-phase state manifests itself in an inclined banding structure of *Imma* phase, and persists from piston velocities of around 1.5 km s$^{-1}$ up to around 2.1 km s$^{-1}$, at which point the structure becomes very disordered indicating shock melting of the sample. By extracting the lattice parameters of the various phases from the Fourier transform images of the real-space atomic positions, and interpreting the banding structure in terms of the relief of shear stress across the plane perpendicular to the shock propagation direction, we are able to predict the volume fraction of the *Imma* phase. Furthermore, an analysis of the relative thermodynamic stability of the two phases by computing their enthalpies from the overall $U_S$-$U_p$ relation deduced from the shock velocities, and from directly recording $U$, $P$, and $V$ within the simulations, are in good mutual agreement, predicting that the mixed-phase region first becomes thermodynamically advantageous in the range of $U_p$ between 1.3 and 1.4 km s$^{-1}$, slightly less than the point of onset detected in the MD simulations.

However, despite the insight that these simulations might afford, we note that it is still the case that our prediction for the value of $U_p$, and hence stress, for the onset of the inelastic behavior, is still considerably higher than that found in experiments [1] ($\approx$1.4 km s$^{-1}$ as opposed to $\approx$0.8 km s$^{-1}$, respectively), and the reasons for this discrepancy remain elusive. It is unlikely that experimental samples have an initial defect density that is sufficiently high to influence the material response, although clearly simulations including initial defects may provide further insight. Alternatively it is conceivable that the Erhart-Albe potential [46] is not fully capturing the material response under shock conditions, and some modifications to the potential may be required. We recall that it is not unknown for other types of potentials that faithfully encapsulate certain aspects of material behavior under ambient conditions, to then fail to reproduce known shock response at higher pressures—a classic example being the potential by Ackland *et al.* for iron [63] that provides a good match to the phonon dispersion curves at ambient pressure and temperature, but cannot capture the $\alpha$-$\epsilon$ transition at 130 kbar, whereas the Voter-Chen potential [64,65], while having a poorer match at ambient conditions, reproduces the phase transition. Finally, we note that with the advent of the DC-CAT facility at the Advanced Photon Source (APS) synchrotron facility [66], and the MEC experimental station at the Light Coherent Light

Source (LCLS) free-electron laser facility [67], there are good prospects for more sophisticated laser-based *in situ* x-ray diffraction experiments that could further our understanding of the shock response of matter at the lattice level.

**ACKNOWLEDGMENTS**

A.H. and G.M. gratefully acknowledge support from AWE. The authors would also like to thank Dr. M. J. Suggit for useful conversations and comments.

[1] W. H. Gust and E. B. Royce, J. Appl. Phys. **42**, 1897 (1971).
[2] W. H. Gust and E. B. Royce, J. Appl. Phys. **43**, 4437 (1972).
[3] A. Mujica, A. Rubio, A. Muñoz, and R. J. Needs, Rev. Mod. Phys. **75**, 863 (2003).
[4] G. J. Ackland, Rep. Prog. Phys. **64**, 483 (2001).
[5] R. Hull, *Properties of Crystalline Silicon* (INSPEC, London, 1999), pp. 89–107.
[6] E. Y. Tonkov and E. G. Ponyatovsky, *Phase Transformations of Elements Under High Pressure* (CRC, Boca Raton, FL, 2005), pp. 96–115.
[7] T. Goto, T. Sato, and Y. Syono, Jpn. J. Appl. Phys. **21**, L369 (1982).
[8] S. J. Turneaure and Y. M. Gupta, Appl. Phys. Lett. **90**, 051905 (2007).
[9] S. J. Turneaure and Y. M. Gupta, Appl. Phys. Lett. **91**, 201913 (2007).
[10] S. D. Gilev and A. M. Trubachev, J. Phys.: Condens. Matt. **16**, 8139 (2004).
[11] G. Rosenberg, J. Phys. Chem. Solids **41**, 561 (1980).
[12] N. L. Coleburn, J. W. Forbes, and H. D. Jones, J. Appl. Phys. **43**, 5007 (1972).
[13] J. S. Wark, R. R. Whitlock, A. Hauer, J. E. Swain, and P. J. Solone, Phys. Rev. B **35**, 9391 (1987).
[14] J. S. Wark, R. R. Whitlock, A. A. Hauer, J. E. Swain, and P. J. Solone, Phys. Rev. B **40**, 5705 (1989).
[15] Y. Hironaka, A. Yazaki, F. Saito, K. G. Nakamura, K. Kondo, H. Takenaka, and M. Yoshida, Appl. Phys. Lett. **77**, 1967 (2000).
[16] A. Loveridge-Smith, A. Allen, J. Belak, T. Boehly, A. Hauer, B. Holian, D. Kalantar, G. Kyrala, R. W. Lee, P. Lomdahl, M. A. Meyers, D. Paisley, S. Pollaine, B. A. Remington, D. C. Swift, S. Weber, and J. S. Wark, Phys. Rev. Lett. **86**, 2349 (2001).
[17] D. H. Kalantar, B. A. Remington, J. D. Colvin, K. O. Mikaelian, S. V. Weber, L. G. Wiley, J. S. Wark, A. Loveridge, A. M. Allen, A. Hauer, and M. A. Meyers, Phys. Plasmas **7**, 1999 (2000).
[18] D. H. Kalantar, J. Belak, E. Bringa, K. Budil, M. Caturla, J. Colvin, M. Kumar, K. T. Lorenz, R. E. Rudd, J. Stölken, A. M. Allen, K. Rosolankova, J. S. Wark, M. A. Meyers, and M. Schneider, Phys. Plasmas **10**, 1569 (2003).
[19] H. Kishimura, A. Yazaki, Y. Hironaka, K. G. Nakamura, and K. Kondo, Appl. Surf. Sci. **207**, 314 (2003).
[20] H. Kishimura, H. Morishita, Y. H. Okano, Y. Hironaka, K.-i. Kondo, K. G. Nakamura, and T. Atou, Phys. Rev. B **74**, 224301 (2006).
[21] K. G. Nakamura, Y. Hironaka, H. Kawano, H. Kishimura, and K. Kondo, Laser Part. Beams **22**, 285 (2004).
[22] D. H. Kalantar, E. A. Chandler, J. D. Colvin, R. Lee, B. A. Remington, S. V. Weber, L. G. Wiley, A. Hauer, J. S. Wark, A. Loveridge, B. H. Failor, M. A. Meyers, and G. Ravichandran, Rev. Sci. Instrum. **70**, 629 (1999).
[23] J. S. Wark, D. Riley, N. C. Woolsey, G. Keihn, and R. R. Whitlock, J. Appl. Phys. **68**, 4531 (1990).
[24] J. S. Wark, Contemp. Phys. **37**, 205 (1996).
[25] D. H. Kalantar, E. Bringa, M. Caturla, J. Colvin, K. T. Lorenz, M. Kumar, J. Stölken, A. M. Allen, K. Rosolankova, J. S. Wark, M. A. Meyers, M. Schneider, and T. R. Boehly, Rev. Sci. Instrum. **74**, 1929 (2003).
[26] H. Kishimura and H. Matsumoto, J. Appl. Phys. **103**, 023505 (2008).
[27] H. Kishimura, H. Matsumoto, and N. N. Thadhani, J. Phys.: Conf. Ser. **215**, 012145 (2010).
[28] I. I. Oleynik, S. V. Zybin, M. L. Elert, and C. T. White, AIP Conf. Proc. **845**, 413 (2005).
[29] J. M. D. Lane and A. P. Thompson, AIP Conf. Proc. **1195**, 1157 (2009).
[30] Y. Lin, R. Perriot, V. V. Zhakhovsky, X. Gu, C. T. White, and I. I. Oleynik, AIP Conf. Proc. **1426**, 1171 (2011).
[31] R. Perriot, Y. Lin, V. V. Zhakhovsky, N. Pineau, J. H. Los, J. B. Maillet, L. Soulard, C. T. White, and I. I. Oleynik, AIP Conf. Proc. **1426**, 1175 (2011).
[32] B. L. Holian, Shock Waves **13**, 489 (2004).
[33] B. L. Holian, Phys. Rev. A **37**, 2562 (1988).
[34] B. L. Holian, Shock Waves **5**, 149 (1995).
[35] K. Kadau, T. C. Germann, P. S. Lomdahl, and B. L. Holian, Science **296**, 1681 (2002).
[36] D. H. Robertson, D. W. Brenner, and C. T. White, Phys. Rev. Lett. **67**, 3132 (1991).
[37] E. M. Bringa, K. Rosolankova, R. E. Rudd, B. A. Remington, J. S. Wark, M. Duchaineau, D. H. Kalantar, J. A. Hawreliak, and J. Belak, Nat. Mater. **5**, 805 (2006).
[38] T. C. Germann, B. L. Holian, P. S. Lomdahl, and R. Ravelo, Phys. Rev. Lett. **84**, 5351 (2000).
[39] B. L. Holian and P. S. Lomdahl, Science **280**, 2085 (1998).
[40] E. M. Bringa, J. U. Cazamias, P. Erhart, J. Stölken, N. Tanushev, B. D. Wirth, R. E. Rudd, and M. J. Caturla, J. Appl. Phys. **96**, 3793 (2004).
[41] A. B. Belonoshko, Science **275**, 955 (1997).
[42] S. J. Plimpton, J. Comp. Phys. **117**, 1 (1995).
[43] J. Tersoff, Phys. Rev. B **37**, 6991 (1988).
[44] J. Tersoff, Phys. Rev. B **38**, 9902 (1988).
[45] J. Tersoff, Phys. Rev. Lett. **56**, 632 (1986).
[46] P. Erhart and K. Albe, Phys. Rev. B **71**, 035211 (2005).
[47] H. Balamane, T. Halicioglu, and W. A. Tiller, Phys. Rev. B **46**, 2250 (1992).
[48] S. J. Cook and P. Clancy, Phys. Rev. B **47**, 7686 (1993).
[49] M. Schaible, Crit. Rev. Solid State **24**, 265 (1999).
[50] S. Izumi and S. Sakai, JSME Int. J. A **47**, 54 (2004).
[51] H. Zhao, Z. Tang, G. Li, and N. R. Aluru, J. Appl. Phys. **99**, 064314 (2006).
[52] I.-H. Lee, J.-W. Jeong, and K. J. Chang, Phys. Rev. B **55**, 5689 (1997).
[53] S. M. Jeong and T. Kitamura, Jpn. J. Appl. Phys. **46**, 5924 (2007).

[54] K. Mizushima, S. Yip, and E. Kaxiras, Phys. Rev. B **50**, 14952 (1994).
[55] S. A. Sous, B. O. Hildmann, and W. A. Kaysser, Phys. Status Solidi A **159**, 343 (1997).
[56] C. L. Kelchner, S. J. Plimpton, and J. C. Hamilton, Phys. Rev. B **58**, 11085 (1998).
[57] G. Kimminau, B. Nagler, A. Higginbotham, W. J. Murphy, N. Park, J. A. Hawreliak, K. Kadau, T. C. Germann, E. M. Bringa, D. H. Kalantar, H. E. Lorenzana, B. A. Remington, and J. S. Wark, J. Phys.: Condens. Matter **20**, 505203 (2008).
[58] M. I. McMahon and R. J. Nelmes, Phys. Rev. B **47**, 8337 (1993).
[59] M. I. McMahon, R. J. Nelmes, N. G. Wright, and D. R. Allan, Phys. Rev. B **50**, 739 (1994).
[60] G. E. Duvall and R. A. Graham, Rev. Mod. Phys. **49**, 523 (1977).
[61] G. E. Duvall, in *Propagation of Shock Waves in Solids*, edited by E. Varley (The American Society of Mechanical Engineers, New York, 1976) p. 97.
[62] A. F. M. Barton and A. P. W. Hodder, Chem. Rev. **73**, 127 (1973).
[63] G. J. Ackland, D. J. Bacon, A. F. Calder, and T. Harry, Philos. Mag. A **75**, 713 (1997).
[64] R. Harrison, A. Voter, and S. Chen, *Atomistic Simulation of Materials: Beyond Pair Potentials* (Plenum, New York, 1989), pp. 219–222.
[65] A. Voter, Los Alamos Unclassified Techn. Rep. **93**, 3901 (1993).
[66] D. E. Moncton, E. Crosbie, and G. K. Shenoy, Rev. Sci. Instrum. **60**, 1403 (1989).
[67] P. Emma, R. Akre, J. Arthur, R. Bionta, C. Bostedt, J. Bozek, A. Brachmann, P. Bucksbaum, R. Coffee, F.-J. Decker, Y. Ding, D. Dowell, S. Edstrom, A. Fisher, J. Frisch, S. Gilevich, J. Hastings, G. Hays, Ph. Hering, Z. Huang, R. Iverson, H. Loos, M. Messerschmidt, A. Miahnahri, S. Moeller, H.-D. Nuhn, G. Pile, D. Ratner, J. Rzepiela, D. Schultz, T. Smith, P. Stefan, H. Tompkins, J. Turner, J. Welch, W. White, J. Wu, G. Yocky, and J. Galayda, Nature Photonics **4**, 641 (2010).